ACS OMEGA

Open Access

http://pubs.acs.org/journal/acsodf

Article

Preparation and Microwave-Absorbing Properties of FeCo Alloys by Condensation Reflux Method

Zhen Liu, Bo Wang,* Shicheng Wei,* Wei Huang, Yujiang Wang, Yi Liang, Junqi Li, Xinyang Wang, and Hongyi Su*

Cite This: *ACS Omega* 2024, 9, 33692−33701

Read Online

ACCESS | Metrics & More | Article Recommendations

ABSTRACT: Five groups of FeCo alloy samples with different atomic ratios of Fe/Co (3:7, 4:6, 5:5, 6:4, 7:3) were prepared using the condensation reflux method. The results indicate that varying the atomic ratios of Fe/Co has a significant impact on the microstructure, electromagnetic parameters, and microwave absorption properties of FeCo alloys. As the Fe atom content increases, the morphology of the FeCo alloys transitions from irregular flower-shaped to uniformly spherical and eventually to lamellar. The attenuation of electromagnetic waves in the five groups of alloys is primarily due to magnetic loss. Among them, Fe_6Co_4 exhibits the best absorption performance, with a minimum reflection loss (RL) value of −35.56 dB at a frequency of 10.40 GHz when the matching thickness is 7.90 mm. Additionally, at a matching thickness of 5.11 mm, the maximum effective absorption bandwidth (EAB) reached 2.56 GHz (15.44−18 GHz).

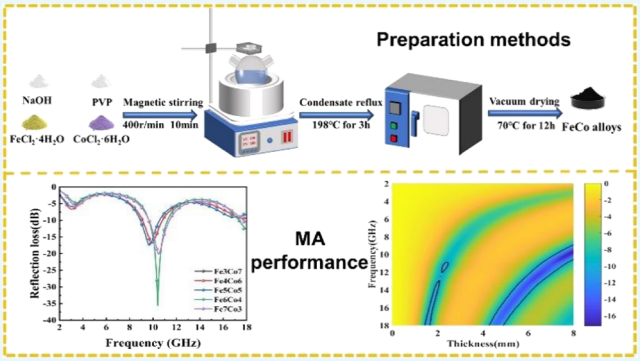

1. INTRODUCTION

The onset of the 5G era has sparked a fresh wave of advancements in electronic technology. While this brings about enhanced convenience in people's daily lives, it also gives rise to a notable increase in electromagnetic pollution, potentially endangering human health.[1−3] Furthermore, as modern warfare escalates, nations are racing to innovate stealth technologies for weaponry and gear to bolster their survivability and operational efficiency in intricate battlefield settings.[4,5] Based on this, efficient microwave absorbers with the advantages of "strong absorption, wide frequency band, lightweight, and thin coating" indeed become a focal point of research in the realm of stealth technology. Currently, reported absorbing materials include magnetic metal particles,[6] ferrite,[7] ceramics,[8] conductive polymer,[9] carbon-based materials,[10−12] and composite materials,[13,14] etc. Undoubtedly, considering the minimum RL, EAB, matching thickness, and corresponding frequency, composite materials outperform the material in terms of absorption effectiveness. Typically, the complex permeability of composite materials is significantly lower than their complex permittivity. In order to further enhance the impedance matching performance of composite materials, there has been widespread interest in materials with strong magnetic loss characteristics in recent years. Among various magnetic loss materials, FeCo alloy has attracted considerable attention as a typical soft magnetic material, offering outstanding magnetic loss performance due to its extremely high saturation magnetization.[15] Furthermore, the high Curie temperature of FeCo alloys establishes the groundwork for their utilization as high-temperature magnetostrictive actuator materials.[16] Additionally, FeCo alloys exhibit favorable economic characteristics and can be prepared by using a variety of methods, making them promising for industrial applications.

Currently, significant research is being conducted on the synthesis of FeCo alloy absorbent materials using hydrothermal and high-energy ball milling methods. Cheng et al.[17] utilized the hydrothermal method to synthesize FeCo alloys with varying atomic ratios. His research revealed that as the Fe atom content increased, the dielectric constant of the FeCo alloys decreased, while the magnetic permeability increased. The resulting Fe_7Co_3 alloy exhibited excellent impedance matching performance and MA effect. By using the hydrothermal synthesis approach for FeCo alloys, our research team explored the influence of different reaction times on the MA properties of FeCo alloys. Our results demonstrate the presence of an optimal reaction time for enhancing the MA

Received: March 10, 2024
Revised: July 11, 2024
Accepted: July 12, 2024
Published: July 24, 2024

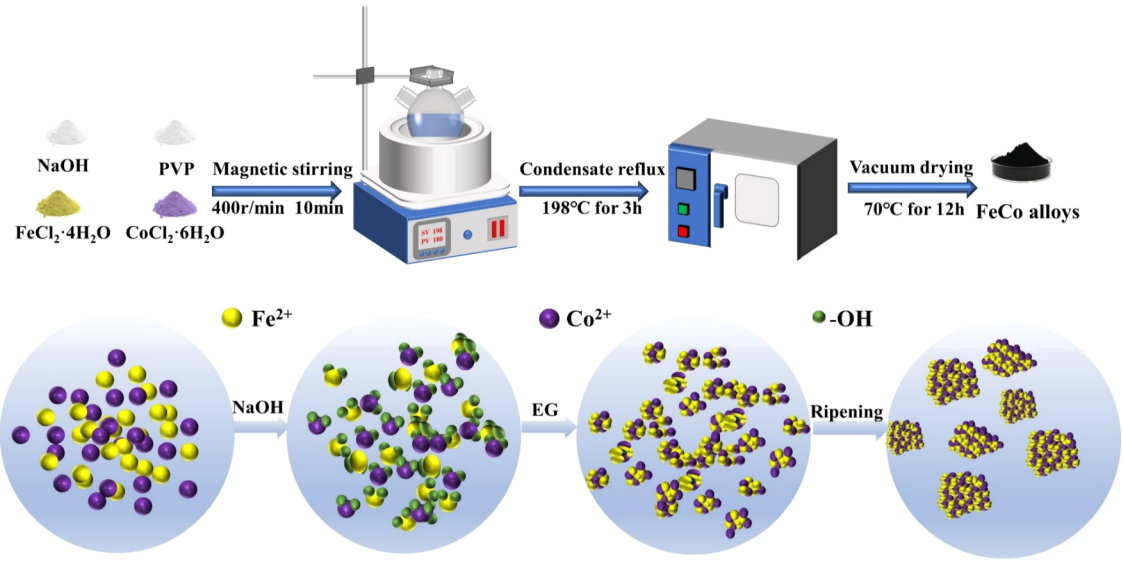

Figure 1. Schematic diagram of FeCo alloy preparation and formation process.

characteristics of FeCo alloys.[18] In addition, Bergheul et al.[19] used a high-energy ball milling method to prepare FeCo powder with an average grain size of 10−13 nm. The alloys obtained the best MA performance at a composition value of 65% Co.

Research on the preparation of the FeCo alloy for MA has been extensive and relatively mature. In addition to the hydrothermal and ball milling methods mentioned earlier, the coprecipitation method is also commonly used. While the hydrothermal and ball milling methods are time-consuming, typically requiring at least 10 h, FeCo alloy particles prepared by the coprecipitation method tend to be relatively large. On the other hand, the condensation reflux method offers a quicker preparation time of approximately 3 h and helps refine the grain size of the FeCo alloy. The condensation reflux method is suitable for both small-scale laboratory preparation and industrial production, showcasing excellent scalability to meet the alloy preparation needs on different scales. But there is no relevant literature on the MA properties of the products prepared by this method. In view of this, FeCo alloys with different atomic ratios were prepared by condensation reflux in this experiment. Through research, it was found that the proportion relationship between Fe and Co atoms has a significant influence on the morphology, magnetism, and overall effectiveness in MA. To be realistic, the FeCo alloy prepared in this experiment does not exhibit outstanding wave absorption performance. Although the FeCo alloy prepared in this experiment did not demonstrate outstanding MA performance, the method proposed presents a new approach for the preparation of the FeCo alloy for MA applications. This highlights the potential for further research and optimization to enhance the MA properties of FeCo alloys prepared by using the condensation reflux method.

2. EXPERIMENTAL SECTION

2.1. Synthesis of FeCo Alloys. Using $FeCl_2·4H_2O$ and $CoCl_2·6H_2O$ as sources of Fe and Co, ensure that the sum of the concentrations of Fe and Co atoms is 0.08 mol/L, and control the atomic ratios of the two to 3:7, 4:6, 5:5, 6:4, and 7:3. 300 mL of ethylene glycol was poured into a three-necked flask placed in a magnetic heating jacket. Under argon protection, add a certain amount of $l_2·4H_2O$, $CoCl_2·6H_2O$, 25 g of NaOH, and 2 g of PVP into the ethylene glycol solution. Stir for 10 min at a rotational speed of 400 r/min, and then begin heating.

The heating temperature is 198 °C (the boiling point of ethylene glycol is 197.4 °C). Consider the time at which heating begins as the starting point and reflux for 3 h.

After the reaction, cool to room temperature with stirring, collect the black precipitates with a magnet, wash them with ethanol and pure water three times each, and vacuum-dry them for 12 h at a temperature of 70 °C. Based on the varying atomic ratios of Fe and Co, the products are recorded as Fe_3Co_7, Fe_4Co_6, Fe_5Co_5, Fe_6Co_4, and Fe_7Co_3. The schematic diagram of the preparation process is shown in Figure 1.

Figure 1 illustrates the process of preparing the FeCo alloy using the condensation reflux method. Initially, Fe^{2+} and Co^{2+} combine with OH^- to form hydroxides ($Fe(OH)_2$ and $Co(OH)_2$). Subsequently, under argon protected condensation reflux conditions, ethylene glycol vapor dynamically releases divalent metal ions from hydroxide precipitation. These divalent metal ions are simultaneously reduced to metal FeCo nuclei due to their very similar reduction potentials, atomic radii, and entropy values. Finally, the alloy core gradually assembles and grows in a heated solution, forming FeCo crystals to reduce surface energy.[20]

2.2. Characterization. In order to analyze the phase of the material under investigation, a high-powered rotating target polycrystalline D8 Advance X-ray diffractometer (XRD) with Cu Kα radiation was used to scan the range 20−100° at a speed of 8°/min. Microstructural and morphological observation was carried out using a Fei Nava Nano450 cold field emission scanning electron microscope (SEM). The Lakeshore 7404 vibrating sample magnetometer (VSM) was utilized for measuring the magnetostatic properties, including saturated magnetization (Ms) and coercive force (Hc). Electromagnetic properties were analyzed across a frequency range of 2−18 GHz employing an Agilent E5071C vector network analyzer (VNA) with a 6:4 mass ratio paraffin mixture. Furthermore, modeling of the RL characteristics of samples with varying thicknesses was achieved through the application of transmission line theory.

https://doi.org/10.1021/acsomega.4c02330
ACS Omega 2024, 9, 33692−33701

3. RESULTS AND DISCUSSION

3.1. Phase Analysis. Figure 2 illustrates the XRD patterns of the FeCo alloys with varying atomic ratios. The diffraction

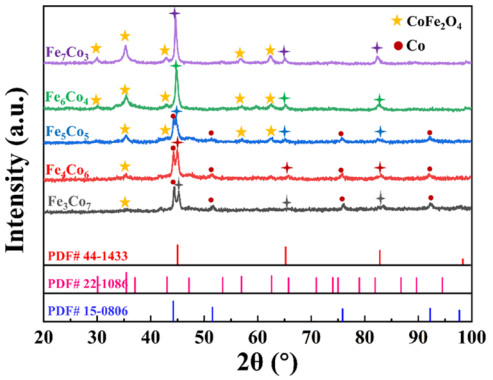

Figure 2. XRD patterns of FeCo alloys with different atomic ratios.

peaks observed at 45.1, 65.5, and 83.2° in all five samples correspond to the (110), (200), and (211) crystal planes of Fe_3Co_7, Fe_4Co_6, Fe_5Co_5, Fe_6Co_4, and Fe_7Co_3 alloys, respectively, as confirmed by comparison with standard reference cards. Notably, the intensity of these peaks exhibits a pattern of initial increase followed by a decrease as the Fe content rises, with Fe_6Co_4 displaying the highest intensities among the set. Additionally, Fe_3Co_7, Fe_4Co_6, and Fe_5Co_5 exhibit peaks at 44.2, 51.5, 75.9, and 92.4°, corresponding to the (111), (200), (220), and (311) crystal planes of Co, with diminishing intensities as the Fe content increases. Furthermore, the peaks detected at 30.1, 35.4, 43, 56.9, and 62.6° are attributed to the (220), (311), (400), (511), and (440) crystal planes of $CoFe_2O_4$, respectively. Notably, the intensities of these peaks exhibit a consistent increase with a rising Fe content. The presence of impurities in the FeCo alloy synthesized via condensation reflux is evident, with the impurity profile varying with the Fe and Co atomic ratios. This phenomenon may be attributed to the presence of trace amounts of oxygen in the ethylene glycol medium. Particularly, when the Co-to-Fe atomic ratio approaches 1:2, the preferential formation of $CoFe_2O_4$ occurs due to the enhanced reactivity between Fe^{3+} and Co^{2+} ions. Conversely, in cases of higher Co content, Co^{2+} ions tend to be reduced to elemental Co, exhibiting reduced susceptibility to oxidation by oxygen within the ethylene glycol vapor environment.[21] Based on the XRD results, it can be inferred that oxygen may have been introduced into the process of generating the FeCo alloy due to factors such as weak sealing. Referring to the final product, the chemical equations that occurred in the medium should include the following

$$Fe^{2+} + Co^{2+} + 4OH^- = Fe(OH)_2 \downarrow + Co(OH)_2 \downarrow \quad (1)$$

$$5Fe(OH)_2 + 5Co(OH)_2 + 2(CH2OH)_2 = 5FeCo + 4CO_2 \uparrow + 16H_2O \quad (2)$$

$$5Co(OH)_2 + (CH2OH)_2 = 5Co + 2CO_2 \uparrow + 8H_2O \quad (3)$$

$$4Fe(OH)_2 + 2Co(OH)_2 + O2 = 2CoFe_2O_4 + 6H_2O \quad (4)$$

3.2. Microstructure Analysis. Figure 3 shows the SEM observations conducted to investigate the impact of varying atomic ratios on the morphology and structure of the FeCo alloys. As depicted in the images, as the Fe atom content increases, the shape of the product gradually transitions from irregular flower-shaped to uniform spherical. The SEM image of Fe_3Co_7 in Figure 3a reveals a structure resembling a flower composed of many small lamellar layers stacked together, making it difficult to distinguish the specific sizes of individual particles. Similarly, the microstructure of Fe_4Co_6 in Figure 3b is akin to that of Fe_3Co_7. In Figure 3c, the SEM image of Fe_5Co_5 shows a mixture of flower-like structures and irregular aggregations, unlike Fe_4Co_6 and Fe_3Co_7. When the Fe atom content reaches its maximum, the spherical products of Fe_7Co_3 aggregate into lamellar shapes, as shown in Figure 3e. Additionally, in Figure 3d, the spherical particle size of the Fe_6Co_4 alloy ranges from 40−50 nm, while other samples exhibit severe aggregation due to their small particle size, hindering clear identification of the specific size. It is confirmed that the FeCo alloy particles produced through the condensation reflux method are all nanoscale particles, which

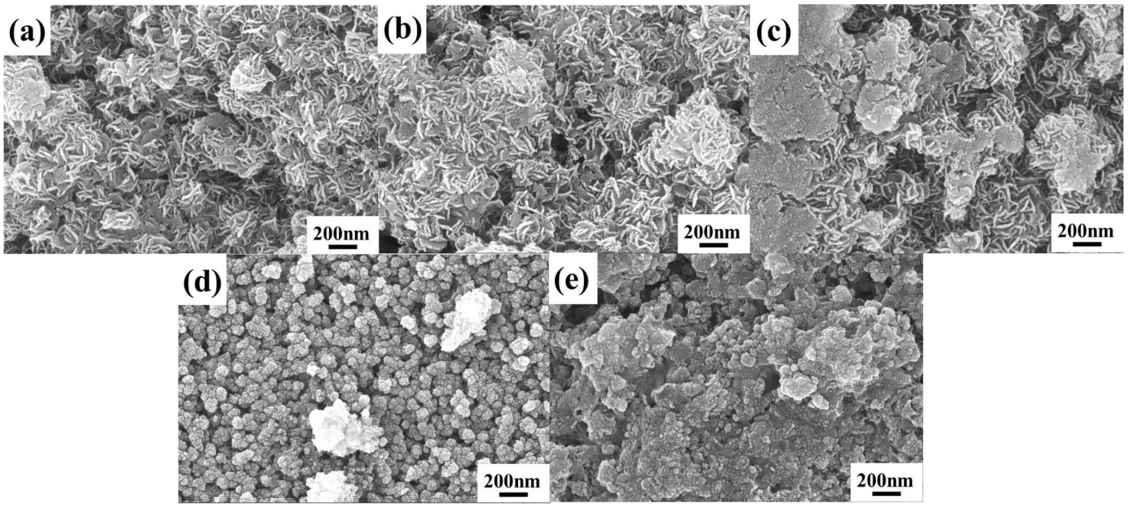

Figure 3. SEM of FeCo alloys with different atomic ratios: (a) Fe_3Co_7, (b) Fe_4Co_6, (c) Fe_5Co_5, (d) Fe_6Co_4, (e) Fe_7Co_3,.

https://doi.org/10.1021/acsomega.4c02330
ACS Omega 2024, 9, 33692−33701

will contribute to promoting magnetic loss due to the exchange resonance.

3.3. Analysis of Magnetostatic Characteristics. In the hysteresis loop, the reverse magnetic field corresponds to the Hc of the material, while the maximum magnetization that a sample can attain upon magnetization in a magnetic field is referred to as the Ms. Figure 4 illustrates the hysteresis loops of

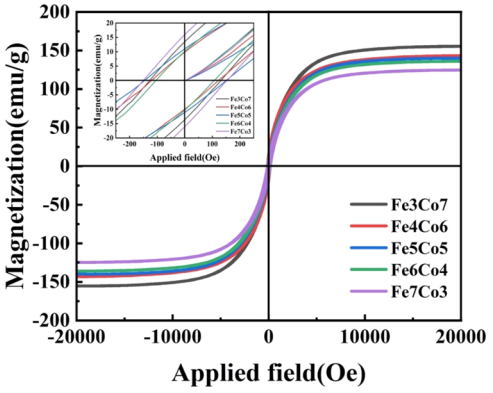

Figure 4. Magnetization curves of FeCo alloys with different atomic ratios.

FeCo alloys with various atomic ratios at room temperature, with the corresponding Ms and Hc values presented in Table 1. It is evident that the Ms of FeCo alloys decreases with

Table 1. Ms and Hc of FeCo Alloys with Different Atomic Ratios

sample	Ms (emu/g)	Hc (Oe)
Fe_3Co_7	155.34	126.14
Fe_4Co_6	143.22	122.72
Fe_5Co_5	139.97	148.75
Fe_6Co_4	135.87	105.29
Fe_7Co_3	124.56	149.75

increasing Fe content. This can be attributed to the continued increase in the $CoFe_2O_4$ impurity content and the concurrent decrease in Co impurity content, as the Ms of Co is significantly higher than that of $CoFe_2O_4$. Upon comparison of the Hc values of the five sample groups, it is observed that Fe_6Co_4 has the smallest Hc. This can be attributed to its spherical and uniformly distributed morphology, which results in a smaller magnetic crystal anisotropy. Consequently, a smaller external magnetic field is required for rotation of the saturation magnetization in the opposite direction, leading to a smaller Hc. The Hc values of Fe_3Co_7 and Fe_4Co_6 are similar, while those of Fe_5Co_5 and Fe_7Co_3 are alike due to the similar morphology and material composition between these groups. Typically, the Ms and coercivity Hc determine the initial magnetic permeability (μ_i). The specific expression is as follows[22]

$$\mu_i = \frac{M_S^2}{akH_CM_S + b\lambda\xi} \tag{5}$$

Wherein, a and b are two constants determined by the composition of the substance, λ is the magnetostrictive coefficient, and ξ is the elastic strain parameter of the crystal. Generally, the relationship between μi and magnetic loss capacity is proportional, meaning that a higher μi can be used to predict a stronger magnetic loss capacity in magnetic MAMs. From the above formula, high Ms and low Hc are beneficial for obtaining a high μ_i. That is, it is beneficial to obtain stronger magnetic loss performance. Based on the above magnetic parameters, it can be inferred that the magnetic loss ability of Fe_3Co_7 may be the strongest, while the magnetic loss ability of Fe_7Co_3 may be the weakest.

3.4. Analysis of Electromagnetic Performance and MA Performance. The ability of absorbing materials to absorb electromagnetic waves depends on its complex relative permittivity ($\varepsilon_r = \varepsilon' - j\varepsilon''$) and complex permeability ($\mu_r = \mu' - j\mu''$). The real parts of these quantities, ε' and μ', represent the material's ability to polarize and magnetize in an alternating electromagnetic field, while the imaginary parts, ε'' and μ'', represent the material's ability to dissipate electrical and magnetic energy.[23−25] Additionally, the material's electrical and magnetic loss capacity can be determined by measuring the tangent value of the dielectric loss angle ($\tan\delta_\varepsilon$) and magnetic loss angle ($\tan\delta_\mu$), respectively, expressed as follows[26]

$$\tan\delta_\varepsilon = \frac{\varepsilon''}{\varepsilon'} \tag{6}$$

$$\tan\delta_\mu = \frac{\mu''}{\mu'} \tag{7}$$

According to Figure 5a,b, it is evident that both the real and imaginary parts of the complex dielectric constants of the five FeCo alloy samples display a clear frequency dispersion. This implies that the dielectric constants of the samples vary as a function of the frequency. Specifically, this behavior indicates that the FeCo alloy experiences dielectric polarization relaxation.[22] As the Fe content increases, the real part of the FeCo alloy's dielectric constant exhibits a downward trend, while the imaginary part presents an upward trend. This may be due to the decreasing number of Co atoms and Co impurities in the alloy, accompanied by an increasing amount of $CoFe_2O_4$ impurities. Compared to Co, both Fe and $CoFe_2O_4$ exhibit stronger attenuation capabilities for electromagnetic waves, with $CoFe_2O_4$ having an even higher electrical loss ability than FeCo alloys.[27] And Co exhibits an exceptional energy storage capacity, making it an ideal material for supercapacitor applications. According to Figure 5c, the curve of the tangent of the dielectric loss angle of the sample varies with frequency in a manner similar to the curve of the imaginary part of its dielectric constant. In the frequency range 2−18 GHz, Fe_7Co_3 exhibits the highest dielectric loss capability, with values ranging from 0.08 to 0.12. This enhanced dielectric loss capability is attributed to the increasing number of Fe atoms and the presence of $CoFe_2O_4$ impurities. The real and imaginary parts of the complex permeability as well as the tangent of the magnetic loss angle for the five samples are depicted in Figures 5d−f. It can be observed that with the continuous increase in Fe content, the real and imaginary parts of the magnetic permeability of FeCo alloys show a decreasing trend. This phenomenon may be attributed to the increasing Fe content leading to a continuous rise in the content of $CoFe_2O_4$, while reducing the Co content.[17,18] However, there exists a discernible disparity in the magnetic loss capabilities between magnetic metal oxides and pure magnetic metal elements.[4] In a similar vein, the curve of the tangential value of the magnetic loss angle closely mirrors the curve of the imaginary part of the magnetic permeability of

https://doi.org/10.1021/acsomega.4c02330
ACS Omega 2024, 9, 33692−33701

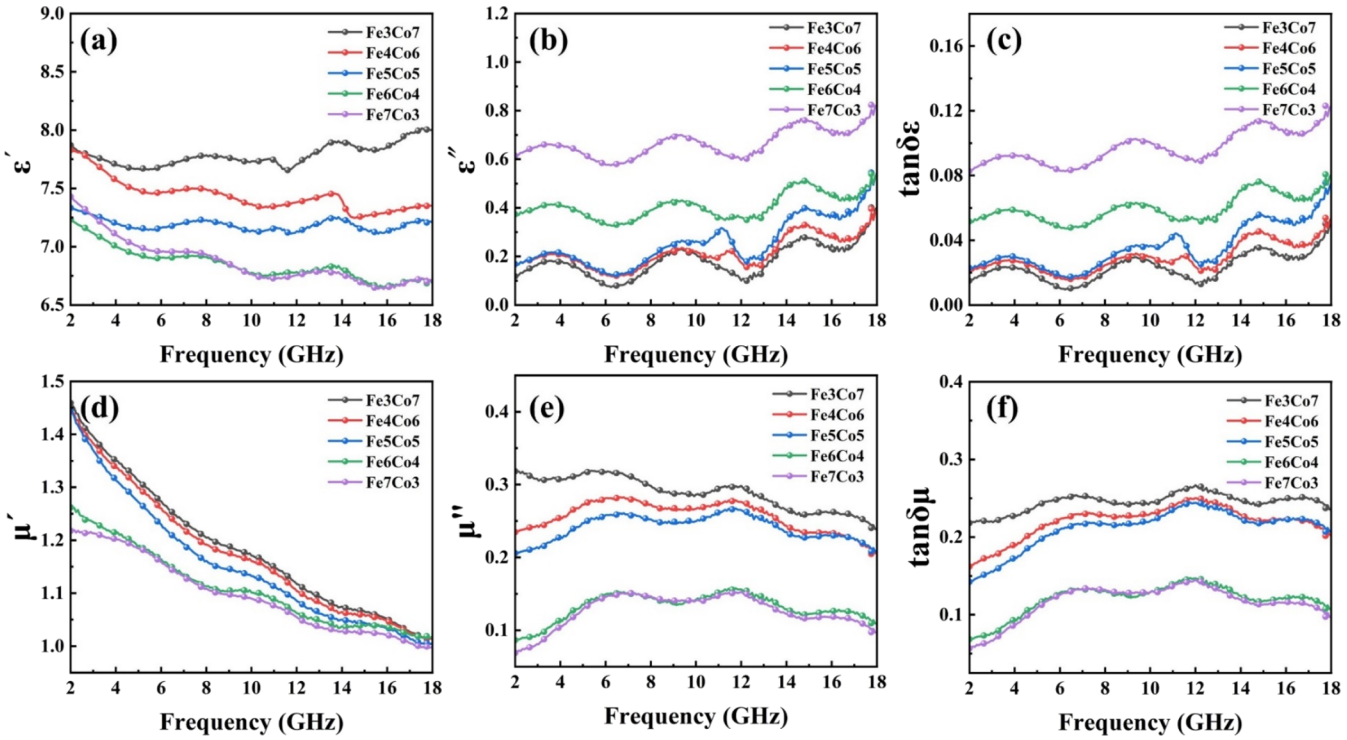

Figure 5. Electromagnetic parameters of FeCo alloys with different atomic ratios: (a) the ε' of 5 samples, (b) the ε'' of 5 samples, (c) the tan δ_ε of 5 samples, (d) the μ' of 5 samples, (e) the μ'' of 5 samples, (f) the tan δ_μ of 5 samples.

the sample. Notably, Fe_3Co_7 exhibits the highest magnetic loss capability, with a specific value ranging between 0.22 and 0.25, aligning well with the conclusions drawn from the magnetization curve.

To visually compare the differences in the absorption properties of FeCo alloys with different atomic ratios, the reflectivity of the samples in the frequency range of 2−18 GHz and the thickness of the absorption layer was simulated using the transmission line theory. The expression for reflectivity is as follows[28]

$$R_L = 20 \log \left| \frac{Z_{in} - Z_0}{Z_{in} + Z_0} \right| \tag{8}$$

$$Z_{in} = Z_0 \sqrt{\frac{\mu_r}{\varepsilon_r}} \tan h\left(j \frac{2fd\pi}{c} \sqrt{\mu_r \varepsilon_r} \right) \tag{9}$$

In the provided equation, Z_{in} represents the input impedance of the material, while f and d stand for the microwave frequency and the thickness of the material, respectively. The speed of light is denoted by c. Normally, the reflectivity RL is expressed as a negative value. An RL value of ≤−10 dB is deemed as effective absorption, suggesting that at least 90% of the electromagnetic waves can be absorbed. This value is known as the effective absorption bandwidth (EAB), which signifies the frequency range of an electromagnetic wave.

The RL diagram of the five groups of samples is depicted in Figure 6a−e. It is evident from the figures that the absorption effectiveness of Fe_6Co_4 surpasses that of the other four sample groups significantly. To further evaluate the absorption capabilities of the five sample groups, the curves illustrating the minimum RL values and the maximum EAB values within the 2−18 GHz range for each group were plotted, as illustrated in Figure 6f,g. Among these, optimal performance is observed when the matching thickness of Fe_6Co_4 is 7.90 mm, resulting in a minimum RL value of −35.56 dB at a frequency of 10.40 GHz. The minimum RL values for the remaining four groups do not exhibit substantial differences, with Fe_3Co_7 and Fe_4Co_6 both achieving minimum RL values at a frequency of 9.92 GHz, measuring −16.91 and −16.92 dB, respectively, with identical matching thicknesses of 7.96 mm. This consistent outcome aligns with the electromagnetic parameters displayed in Figure 4, indicating close proximity. However, the slight variations in microscopic morphology and impurity content between these two sample groups may underlie this outcome. Fe_7Co_3 demonstrates a minimum RL value performance slightly below that of Fe_6Co_4, with a minimum RL value of −20.18 dB recorded at 10.48 GHz when the matching thickness is 7.9 mm. For Fe_5Co_5, a minimum RL value of −17.18 dB is achieved at a frequency of 9.76 GHz with a matching thickness of 7.95 mm. Regarding the maximum EAB, the performance of the five samples is relatively consistent. The matching thickness for all five sample groups ranges from 4.85 to 5.15 mm, with the maximum EAB falling around 2.64 GHz (15.36−18 GHz). This indicates that the samples demonstrate outstanding performance at higher frequencies, possibly attributed to the small particle size of the prepared FeCo alloy, making it susceptible to exchange resonance at high frequencies.[25] To be candid, the FeCo alloy prepared in this experiment does not hold an advantage over the reported magnetic MAMs in terms of the minimum RL, EAB, or matching thickness. The reason for this situation may be oxidation of the material during the preparation process. On one hand, the oxygen in the solution may not have been completely removed, and on the other hand, the poor sealability of the equipment allowed oxygen to enter during the sample preparation. The oxidation phenomenon during the

https://doi.org/10.1021/acsomega.4c02330
ACS Omega 2024, 9, 33692−33701

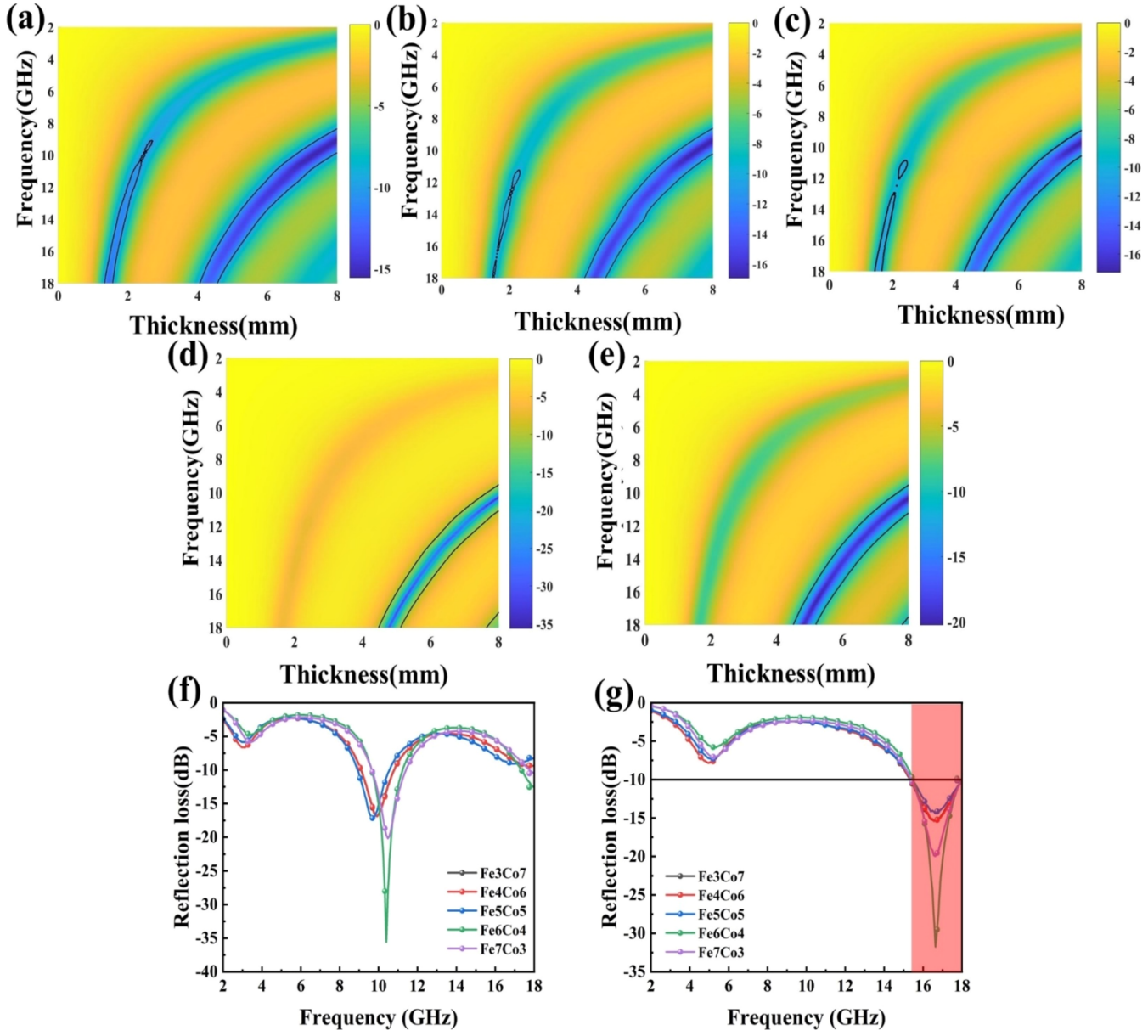

Figure 6. (a–e) Top view of RL values for Fe_3Co_7, Fe_4Co_6, Fe_5Co_5, Fe_6Co_4, and Fe_7Co_3. (f) Optimal RL values for 5 samples, and (g) maximum EAB of 5 samples.

preparation process resulted in the presence of impurities such as $CoFe_2O_4$ in the obtained FeCo alloy, which ultimately led to poor MA performance.

3.5. Analysis of MA Mechanism. To investigate the magnetic absorption mechanism of FeCo alloy prepared by the condensation reflux method, the dielectric loss and magnetic loss characteristics of the FeCo alloy were analyzed using the Cole–Cole diagram and the curve of the C_0 value versus frequency.

The Debye semicircle in the Cole–Cole diagram reflects the dielectric's spectral characteristics of polarization as well as the extent to which it deviates from Debye relaxation. This diagram is commonly used to illustrate the polarization relaxation characteristics of dielectric constants.[29] The Cole–Cole diagram is derived from the Debye equation, which describes the relationship between the real and imaginary parts of the dielectric constant. Specifically, the equation expresses this relationship as follows[6]

$$\varepsilon' = \varepsilon_\infty + \frac{\varepsilon_s - \varepsilon_\infty}{1 + iw^2\tau^2} \tag{10}$$

$$\varepsilon'' = \varepsilon_\infty + \frac{w\tau(\varepsilon_s - \varepsilon_\infty)}{1 + iw^2\tau^2} \tag{11}$$

$$\left(\varepsilon' - \frac{\varepsilon_S + \varepsilon_\infty}{2}\right)^2 + (\varepsilon)''^2 = \left(\frac{\varepsilon_S - \varepsilon_\infty}{2}\right)^2 \tag{12}$$

The Debye equation establishes a connection between the real and imaginary components of the dielectric constant with ε_S and ε_∞ denoting the dielectric constants at static and high-frequency limits, respectively. When a material undergoes dielectric polarization relaxation within a specific frequency range, its ε' and ε'' values conform to the Debye relaxation model, resulting in the formation of a Cole–Cole semicircle. The semicircle's radius in the Cole–Cole diagram is directly linked to the extent of dielectric polarization relaxation

https://doi.org/10.1021/acsomega.4c02330
ACS Omega 2024, 9, 33692–33701

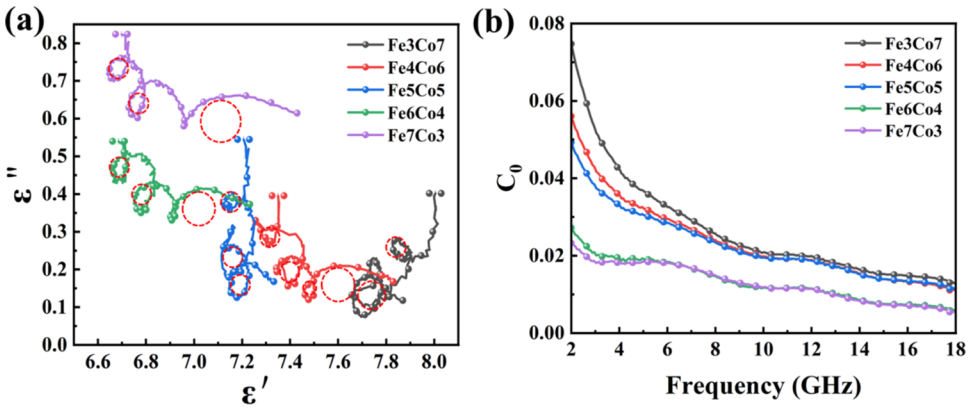

Figure 7. Various properties of FeCo alloys with different atomic ratios: (a) Cole−Cole diagram and (b) the curve of C_0 value.

exhibited by the material. Therefore, a semicircle depicted on the Cole−Cole diagram signifies a polarization relaxation process.[30] As depicted in Figure 7a, multiple semicircles are evident in all five sample groups, signifying the occurrence of multiple polarization relaxation processes within the frequency range of 2−18 GHz. These relaxation processes encompass interfacial polarization arising from distinct interfaces and dipole polarization stemming from defects within the particles themselves. Furthermore, it was observed that as the Fe content progressively increased, the Debye semicircle diameter of the five sample groups also increased continuously, with the longitudinal coordinate of the circle's center experiencing a corresponding rise. This trend indicates a continuous enhancement in the relaxation strength and conductivity of the samples, possibly attributed to the escalating $CoFe_2O_4$ content accompanying the increase in the Fe content. This augmentation improved the conductivity and furnished a greater number of heterogeneous interfaces, intensifying the interfacial polarization phenomenon. This observation aligns with the variation trend of the dielectric loss angle tangent value illustrated in Figure 5c.

The magnetic losses of wave-absorbing materials generally include hysteresis losses, magnetic domain resonance, natural resonance, exchange resonance, and eddy current losses. Hysteresis loss generally occurs in the range of 1−104 Hz, and magnetic domain resonance occurs in the range of 1−100 MHz.[17] The magnetic losses of wave-absorbing materials typically encompass hysteresis losses and magnetic domain resonance. In the frequency range 2−18 GHz, the magnetic losses of microwave-absorbing materials are mainly attributed to eddy current losses, natural resonance losses, and exchange resonance losses. The FeCo alloy used in this experiment is classified as a soft magnetic material with magnetocrystalline anisotropy, thus meeting the conditions for natural resonance to manifest. Additionally, the presence of numerous nanoscale particles in FeCo alloys can induce a higher exchange resonance compared to natural resonance. For eddy current losses, the main influencing factors include conductivity (σ) and the material thickness (d), whose expression is as follows[15]

$$C_0 = \mu''(\mu')^{-2} f^{-1} = \frac{2}{3}\pi\mu_0 d^2\sigma \tag{13}$$

The given equation involves the variable f, which represents the frequency of the electromagnetic wave, and μ_0, which is the vacuum magnetic permeability. This equation shows that if the magnetic loss of an absorbing material mainly comes from eddy current losses, the value of C_0 should remain relatively constant or change minimally. As shown in Figure 7b, the C_0 values of the five sets of samples basically remain unchanged in the frequency range of 14−18 GHz. The magnetic loss of the FeCo alloy to electromagnetic waves is to some extent caused by eddy current losses. At this time, electromagnetic waves are at high frequencies, leading to the generation of stronger induced currents, a decrease in conductivity, an increase in resistivity, and the formation of stronger eddy current losses. In addition, there are also significant peaks in the frequency range of 10−14 GHz, which are caused by the natural resonance of FeCo alloy particles' magnetic crystal anisotropy and the exchange resonance generated by electron spin magnetic moments.

In order to analyze the absorption mechanism of the FeCo alloy more deeply, the quarter-wavelength matching theory was used to elucidate the relationship between thickness and frequency. This theory refers to the destructive interference that occurs when the amplitudes of the electromagnetic waves reflected at the internal and external interfaces of the absorbing coating are equal and the phase satisfies a quarter wavelength. That is, when the thickness of the absorbing material satisfies a quarter-wavelength relationship, the two waves cancel each other out. To comprehensively assess the absorption mechanism of the FeCo alloy, the impedance matching performance and attenuation coefficient of the samples were analyzed simultaneously. The normalized impedance coefficient Z is an effective method for evaluating the impedance matching situation at a specific thickness. A Z value closer to 1 indicates reduced reflection of electromagnetic waves and improved impedance matching performance of the material.[31] The attenuation coefficient (α) is a key indicator that measures the ability of absorbing materials to reduce the incident electromagnetic microwave energy. A higher α value indicates stronger electromagnetic wave loss within the material. The specific formulas for the three are as follows[32−34]

$$t_m = nc/(4f_m(|\mu_r||\varepsilon_r|)^{1/2}) \qquad (n = 1, 3, 5...) \tag{14}$$

$$\alpha = \frac{\sqrt{2}\,\pi f}{C}\sqrt{\mu''\varepsilon''\text{-}\mu'\varepsilon' + \sqrt{(\mu''\varepsilon''\text{-}\mu'\varepsilon')^2 + (\varepsilon'\mu'' + \varepsilon''\mu')^2}} \tag{15}$$

$$Z = \left|\frac{Z_{in}}{Z_0}\right| = \sqrt{\left|\frac{\mu_r}{\varepsilon_r}\right|}\tan h\left[j\frac{2\pi df}{c}\sqrt{\mu_r\varepsilon_r}\right] \tag{16}$$

https://doi.org/10.1021/acsomega.4c02330
ACS Omega 2024, 9, 33692−33701

Where f is the frequency, λ is the wavelength, and c is the speed of light. The reflection loss diagram of Fe_6Co_4 (as shown in Figure 8a) shows that with increasing thickness, the

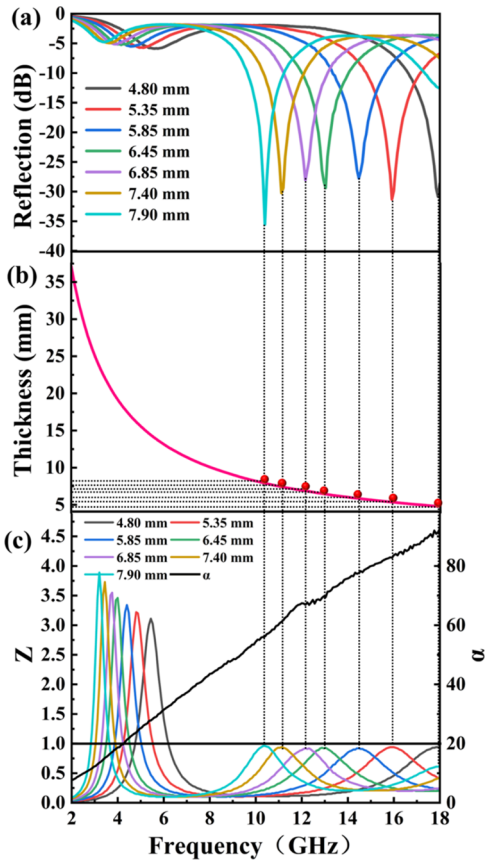

Figure 8. (a) The reflection loss curves of Fe_6Co_4, (b) the corresponding different simulated thickness, and (c) the impedance matching (Z value) at the simulated thickness and the attenuation constant (α).

reflection loss value shifts toward lower frequencies. All experimental thicknesses obtained from the reflection loss are shown as red circles in Figure 8b, which match well with the simulated thickness. This indicates that the prepared FeCo alloy conforms well to the quarter-wavelength matching theory. Figure 8c shows the reflection loss at different thicknesses corresponding to impedance matching and attenuation coefficients. It can be seen that when Fe_6Co_4 achieves the lowest reflection loss value, even if its attenuation coefficient value is not optimal, the corresponding impedance matching performance is the best. In addition, within the range of 3−7 GHz, although Fe_6Co_4 exhibits optimal matching performance at different matching thicknesses, excessively small attenuation coefficients also do not result in superior reflection loss. It can be seen that the absorption performance of the prepared FeCo alloy is determined by the comprehensive impedance matching performance and the attenuation coefficient.

Based on the analysis above, the electromagnetic wave absorption mechanism of the FeCo alloy mainly relies on magnetic loss, supplemented by a certain degree of dielectric loss. In addition, the electromagnetic wave absorption of the FeCo alloy follows the quarter-wavelength theory. The MA mechanism diagram (see Figure 9) indicates that the FeCo alloy prepared by the condensation reflux method is composed

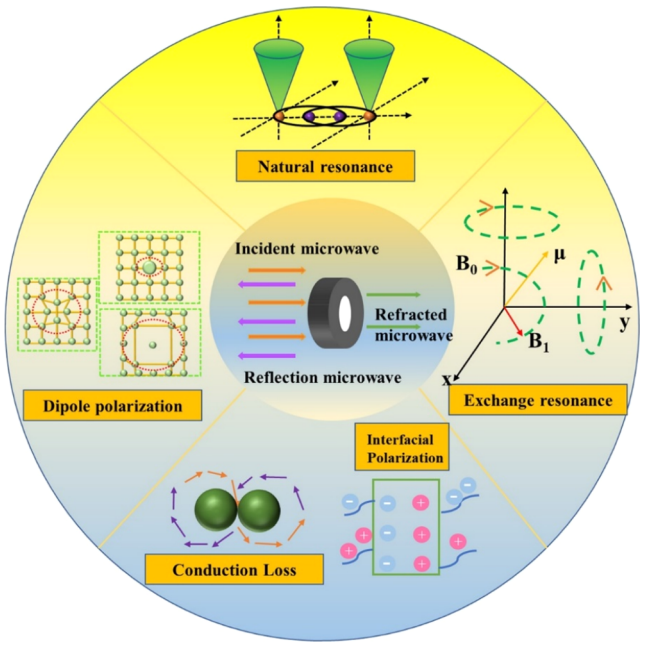

Figure 9. Schematic diagram of MA mechanism of the FeCo alloy.

of many nanoscale particles with strong magnetic crystal anisotropy. On the one hand, when strong magnetic crystal anisotropy exists in the nanoscale particles, the direction of the magnetic moment is restricted, causing the magnetic moment to undergo precession under exchange coupling, thereby forming deep exchange resonance.[35,36] On the other hand, strong magnetic crystal anisotropy changes the natural frequency of the magnetic moment in the nanoscale particles, making it easier for the magnetic moment to achieve resonant absorption under an applied alternating magnetic field.[37] According to the C_0 curve, all five sets of samples exhibit a certain level of eddy current loss capability. In terms of dielectric loss, conduction loss is the key to its dielectric loss. The lattice structure of the FeCo alloy is relatively dense, and the movement of electrons in the lattice is less hindered, which is conducive to electron transport and thus improves electrical conductivity. Furthermore, impurities in the material, compounds of different substances, and irregular shapes generate different electrical properties at interfaces, leading to interface polarization.[38] Meanwhile, various point defects such as vacancies and interstitial atoms exist in the FeCo alloy. These point defects can cause lattice imperfections, leading to lattice distortion. These situations can induce dipole polarization phenomena, such as the introduction of local charge imbalance by point defects, leading to the formation of local dipole moments around the lattice. These dipole moments interact with each other, causing irregular distribution of dipole moments in the lattice, thereby triggering dipole polarization relaxation.[39]

4. CONCLUSIONS

Utilizing the condensation reflux method for the preparation of FeCo alloys, five sets of FeCo alloys were successfully synthesized by controlling varying atomic ratios of Fe/Co. The study reveals that these different atomic ratios of Fe/Co significantly influence the morphology and structure of the resulting products. Notably, when the Fe/Co atomic ratio is 6:4, a uniformly spherical product can be achieved. As per the

https://doi.org/10.1021/acsomega.4c02330
ACS Omega 2024, 9, 33692−33701

aforementioned analysis, the varying atomic ratios of Fe and Co play a crucial role in the attenuation coefficient, impedance matching performance, and ultimate MA effect of the product. Through a comparative assessment of the electromagnetic parameters and MA properties of the three sample groups, it is evident that the electromagnetic wave absorption of the FeCo alloy prepared using this method is primarily dominated by magnetic loss, complemented by electrical loss. Specifically, the most effective absorption is observed when the Fe/Co atomic ratio in the product is 6:4. At a matching thickness of 7.90 mm for Fe_6Co_4, the RL reaches a minimum value of −35.56 dB at a frequency of 10.40 GHz. Furthermore, with a matching thickness of 5.11 mm for Fe_6Co_4, the maximum EAB is measured at 2.56 GHz (ranging from 15.44 to 18 GHz). Certainly, there are limitations to this experiment. On one hand, the issue of sample oxidation during the preparation process has not been effectively resolved, resulting in poor MA performance. On the other hand, there is a lack in the analysis of the samples' microstructure. In future research, we will focus on the impact of the microstructure on microwave absorption performance, further improve the sealability of the preparation equipment to prevent sample oxidation, and strive to significantly enhance the MA capabilities.

■ ASSOCIATED CONTENT

Data Availability Statement

Because the data supporting the findings of this study has been patented and authorized, if you wish to obtain the data from this experiment, you can do so by contacting the corresponding author and stating the reason.

■ AUTHOR INFORMATION

Corresponding Authors

Bo Wang − *National Key Laboratory for Remanufacturing, Army Academy of Armored Forces, Beijing 100072, P. R. China*; orcid.org/0000-0003-3791-2727; Email: wangbobo421@163.com

Shicheng Wei − *National Key Laboratory for Remanufacturing, Army Academy of Armored Forces, Beijing 100072, P. R. China*; Email: scwei33333@163.com

Hongyi Su − *State Key Laboratory of NBC Protection for Civilians, Beijing 100072, P. R. China*; Email: Hongyi@163.com

Authors

Zhen Liu − *National Key Laboratory for Remanufacturing, Army Academy of Armored Forces, Beijing 100072, P. R. China*

Wei Huang − *Department of Naval Architecture Engineering, Naval University of Engineering, Wuhan 430033, P. R. China*

Yujiang Wang − *National Key Laboratory for Remanufacturing, Army Academy of Armored Forces, Beijing 100072, P. R. China*

Yi Liang − *National Key Laboratory for Remanufacturing, Army Academy of Armored Forces, Beijing 100072, P. R. China*

Junqi Li − *National Key Laboratory for Remanufacturing, Army Academy of Armored Forces, Beijing 100072, P. R. China*

Xinyang Wang − *National Key Laboratory for Remanufacturing, Army Academy of Armored Forces, Beijing 100072, P. R. China*

Complete contact information is available at: https://pubs.acs.org/10.1021/acsomega.4c02330

Author Contributions

All authors contributed to the study conception and design. Material preparation, data collection, and analysis were performed by Z.L., B.W., and W.H. The first draft of the manuscript was written by Z.L. and all authors commented on previous versions of the manuscript. All authors read and approved the final manuscript.

Notes

The authors declare no competing financial interest.

■ ACKNOWLEDGMENTS

Thanks for the financial supports from the National Natural Science Foundation of China (Project 51905543), National Defense Science and Technology Excellence Young Scientists Foundation (2017-JCJQ-ZQ-001).

■ REFERENCES

(1) Lv, H.; Yang, Z.; Xu, H.; Wang, L.; Wu, R. An Electrical Switch-Driven Flexible Electromagnetic Absorber. *Adv. Funct Mater.* **2020**, *30*, No. 1907251.

(2) Darovskikh, S. N.; Shonazarov, P. M.; Sodik, F.; Kholov, F. T.; Umaralizoda, R.; Juraeva, R. On the possible causal relationship of the COVID-19 viral disease with electromagnetic pollution of the environment and the main directions of its weakening. *J. Phys: Conf Ser.* **2021**, *1889*, No. 052028.

(3) Litvak, E.; Foster, K. R.; Repacholi, M. H. Health and safety implications of exposure to electromagnetic fields in the frequency range 300 Hz to 10 MHz. *Bioelectromagnetics* **2002**, *23*, 68−82.

(4) Cai, Y.; Yu, H.; Cheng, L.; Guo, S.; Liu, T.; Chen, D.; et al. Structure Design, Surface Modification, and Application of CNT Microwave-Absorbing Composites. *Adv. Sustainable Systems* **2023**, *7*, No. 2300272.

(5) Li, J.; Wei, Y.; Huang, M.; Gao, W.; Yao, K.; Ma, H. Dually inner-porous composites with Co@C prismatic rods anchored into graphene aerogel toward superior electromagnetic wave absorbing materials. *J. Alloys Compd.* **2024**, *970*, No. 172449.

(6) Zhao, H.-B.; Cheng, J.-B.; Zhu, J.-Y.; Wang, Y.-Z. Ultralight CoNi/rGO aerogels toward excellent microwave absorption at ultrathin thickness. *J. Mater. Chem. C* **2019**, *7*, 441−448.

(7) Zhang, T.; Li, Z.; Wang, L.; Zhang, Z.; Wang, S. Spinel CoFe2O4 supported by three dimensional graphene as high-performance bi-functional electrocatalysts for oxygen reduction and evolution reaction. *Int. J. Hydrogen Energy* **2019**, *44*, 1610−1619.

(8) Song, L.; Zhang, F.; Chen, Y.; Guan, L.; Zhu, Y.; Chen, M.; et al. Multifunctional SiC@SiO2 Nanofiber Aerogel with Ultrabroadband Electromagnetic Wave Absorption. *Nano-Micro Lett.* **2022**, *14*, 152.

(9) Peymanfar, R.; Dogari, H.; Selseleh-Zakerin, E.; Hedayatzadeh, M. H.; Daneshvar, S.; Amiri-Ramsheh, N.; et al. Recent advances in microwave-absorbing materials fabricated using organic conductive polymers. *Front Mater.* **2023**, *10*, No. 1133287.

(10) Zhao, B.; Li, Y.; Ji, H.; Bai, P.; Wang, S.; Fan, B.; et al. Lightweight graphene aerogels by decoration of 1D CoNi chains and CNTs to achieve ultra-wide microwave absorption. *Carbon* **2021**, *176*, 411−420.

(11) Huang, W.; Wei, S.; Wang, Y.; Wang, B.; Liang, Y.; Huang, Y.; Xu, B. A New Broadband and Strong Absorption Performance FeCO3/RGO Microwave Absorption Nanocomposites. *Materials* **2019**, *12*, 2206.

(12) Cao, Y.; Cheng, Z.; Wang, R.; Liu, X.; Zhang, T.; Fan, F.; Huang, Y. Multifunctional graphene/carbon fiber aerogels toward compatible electromagnetic wave absorption and shielding in gigahertz and terahertz bands with optimized radar cross section. *Carbon* **2022**, *199*, 333−346.

(13) Li, J.; Yang, S.; Jiao, P.; Peng, Q.; Yin, W.; Yuan, Y.; et al. Three-dimensional macroassembly of hybrid C@CoFe nanoparticles/reduced graphene oxide nanosheets towards multifunctional foam. *Carbon* **2020**, *157*, 427−436.
(14) Wang, L.; Liu, H.; Lv, X.; Cui, G.; Gu, G. Facile synthesis 3D porous MXene Ti3C2Tx@RGO composite aerogel with excellent dielectric loss and electromagnetic wave absorption. *J. Alloys Compd.* **2020**, *828*, No. 154251.
(15) Wan, Y.; Cui, T.; Xiao, J.; Xiong, G.; Guo, R.; Luo, H. Engineering carbon fibers with dual coatings of FeCo and CuO towards enhanced microwave absorption properties. *J. Alloys Compd.* **2016**, *687*, 334−341.
(16) Koutsopoulos, S.; Barfod, R.; Eriksen, K. M.; Fehrmann, R. Synthesis and characterization of iron-cobalt (FeCo) alloy nanoparticles supported on carbon. *J. Alloys Compd.* **2017**, *725*, 1210−1216.
(17) Cheng, Y.; Ji, G.; Li, Z.; Lv, H.; Liu, W.; Zhao, Y.; et al. Facile synthesis of FeCo alloys with excellent microwave absorption in the whole Ku-band: Effect of Fe/Co atomic ratio. *J. Alloys Compd.* **2017**, *704*, 289−295.
(18) Liu, Z.; Wang, B.; Wei, S.; Huang, W.; Wang, Y.; Liang, Y. Hydrothermal synthesis of FeCo alloys with excellent microwave Absorption: Effect of reaction time. *J. Magn. Magn. Mater.* **2023**, *568*, No. 170365.
(19) Bergheul, S.; Haddad, A.; Tafat, A.; Azzaz, M. Magnetic microwave and absorbing properties of Fe-Co alloy synthesised by mechanical alloying process. *IJMMP* **2006**, *1*, 334.
(20) Yang, B.; Fang, J.; Xu, C.; Cao, H.; Zhang, R.; Zhao, B.; et al. One-Dimensional Magnetic FeCoNi Alloy Toward Low-Frequency Electromagnetic Wave Absorption. *Nano-Micro Lett.* **2022**, *14*, 170.
(21) Lee, S. J.; Cho, J.-H.; Lee, C.; Cho, J.; Kim, Y.-R.; Park, J. K. Synthesis of highly magnetic graphite-encapsulated FeCo nanoparticles using a hydrothermal process. *Nanotechnology* **2011**, *22*, No. 375603.
(22) Wu, Y.; Zhao, Y.; Zhou, M.; Tan, S.; Peymanfar, R.; Aslibeiki, B.; Ji, G. Ultrabroad Microwave Absorption Ability and Infrared Stealth Property of Nano-Micro CuS@rGO Lightweight Aerogels. *Nano-Micro Lett.* **2022**, *14*, 171.
(23) Li, Z.; Li, X.; Zong, Y.; Tan, G.; Sun, Y.; Lan, Y.; et al. Solvothermal synthesis of nitrogen-doped graphene decorated by superparamagnetic Fe3O4 nanoparticles and their applications as enhanced synergistic microwave absorbers. *Carbon* **2017**, *115*, 493−502.
(24) Lee, J.-H.; Kim, Y.-S.; Ru, H.-J.; Lee, S.-Y.; Park, S.-J. Highly Flexible Fabrics/Epoxy Composites with Hybrid Carbon Nanofillers for Absorption-Dominated Electromagnetic Interference Shielding. *Nano-Micro Lett.* **2022**, *14*, 188.
(25) Li, J.; Ji, H.; Xu, Y.; Zhang, J.; Yan, Y. Three-dimensional graphene supported Fe3O4 coated by polypyrrole toward enhanced stability and microwave absorbing properties. *J. Mater. Res. Technol.* **2020**, *9*, 762−772.
(26) Zeng, Z.; Wang, G.; Wolan, B. F.; Wu, N.; Wang, C.; Zhao, S.; et al. Printable Aligned Single-Walled Carbon Nanotube Film with Outstanding Thermal Conductivity and Electromagnetic Interference Shielding Performance. *Nano-Micro Lett.* **2022**, *14*, 179.
(27) Zhang, T.; Li, Z.; Wang, L.; Zhang, Z.; Wang, S. Spinel CoFe2O4 supported by three dimensional graphene as high-performance bi-functional electrocatalysts for oxygen reduction and evolution reaction. *Int. J. Hydrogen Energy* **2019**, *44*, 1610−1619.
(28) Wang, Y.; Haidry, A. A.; Liu, Y.; Raza, A.; Duan, L.; He, C.; Zhou, J. Enhanced electromagnetic wave absorption using bimetallic MOFs-derived TiO2/Co/C heterostructures. *Carbon* **2024**, *216*, No. 118497.
(29) Zou, L.; Xiao, X.; Chu, C.; Chen, B. Facile synthesis of porous CoFe2O4/graphene aerogel for catalyzing efficient removal of organic pollutants. *Sci. Total Environ.* **2021**, *775*, No. 143398.
(30) Liu, T.; Huang, L.; Wang, X.; Yin, F.; Yuan, Y. A strong insulating, compressible Nd2O3@CNFs WPU foam for robust electromagnetic wave absorption. *J. Alloys Compd.* **2024**, *975*, No. 172983.
(31) Jiang, Q.; Li, H.; Cao, Z.; Li, H.; Wang, Q.; Jiang, Z.; et al. Synthesis and enhanced electromagnetic wave absorption performance of amorphous CoxFe10-x alloys. *J. Alloys Compd.* **2017**, *726*, 1255−1261.
(32) Fu, X.-Y. Vertically implanting MoSe2 nanosheets on the RGO sheets towards excellent multi-band microwave absorption. *Carbon* **2022**, *197*, 324−333.
(33) Keykavous-Amand, S.; Peymanfar, R. Fabrication of clay soil/CuFe2O4 nanocomposite toward improving energy and shielding efficiency of buildings. *Sci. Rep.* **2021**, *11*, No. 20832.
(34) Qin, M.; Zhang, L.; Wu, H. Dielectric Loss Mechanism in Electromagnetic Wave Absorbing Materials. *Adv. Sci.* **2022**, *9*, 2105553 DOI: 10.1002/advs.202105553.
(35) Guan, X. The controllable porous structure and s-doping of hollow carbon sphere synergistically act on the microwave attenuation. *Carbon* **2022**, *188*, 1−11, DOI: 10.1016/j.carbon.2021.11.045.
(36) Chen, G.; Zhang, L.; Luo, B.; et al. Optimal control of the compositions, interfaces, and defects of hollow sulfide for electromagnetic wave absorption. *J. Colloid Interface Sci.* **2022**, *607*, 24 DOI: 10.1016/j.jcis.2021.08.186.
(37) Zhang, H.; Cheng, J.; Wang, H.; Huang, Z.; Zheng, Q.; Zheng, G.; et al. Initiating VB-Group Laminated NbS2 Electromagnetic Wave Absorber toward Superior Absorption Bandwidth as Large as 6.48 GHz through Phase Engineering Modulation. *Adv. Funct Mater.* **2022**, *32*, 2108194 DOI: 10.1002/adfm.202108194.
(38) Liang, L.; Gu, W.; Wu, Y.; Zhang, B.; Wang, G.; Yang, Y.; Ji, G. Heterointerface Engineering in Electromagnetic Absorbers: New Insights and Opportunities. *Adv. Mater.* **2022**, *34*, 2106195 DOI: 10.1002/adma.202106195.
(39) Wu, Z.; Cheng, H.-W.; Jin, C.; Yang, B.; Xu, C.; Pei, K.; et al. Dimensional Design and Core−Shell Engineering of Nanomaterials for Electromagnetic Wave Absorption. *Adv. Mater.* **2022**, *34*, 2107538 DOI: 10.1002/adma.202107538.

https://doi.org/10.1021/acsomega.4c02330
ACS Omega 2024, 9, 33692−33701